

Article

Not peer-reviewed version

---

# Mineral Deposition on the Rough Walls of a Fracture

---

[Nathann Teixeira Rodrigues](#) , Ismael S. S. Carrasco , [Vaughan R. Voller](#) , [Fábio D. A. Aarão Reis](#) \*

Posted Date: 26 October 2024

doi: 10.20944/preprints202410.2019.v1

Keywords: carbon mineralization; calcite; growth; fracture; Kinetic Monte Carlo; surface steps



Preprints.org is a free multidiscipline platform providing preprint service that is dedicated to making early versions of research outputs permanently available and citable. Preprints posted at Preprints.org appear in Web of Science, Crossref, Google Scholar, Scilit, Europe PMC.

Copyright: This is an open access article distributed under the Creative Commons Attribution License which permits unrestricted use, distribution, and reproduction in any medium, provided the original work is properly cited.

Disclaimer/Publisher's Note: The statements, opinions, and data contained in all publications are solely those of the individual author(s) and contributor(s) and not of MDPI and/or the editor(s). MDPI and/or the editor(s) disclaim responsibility for any injury to people or property resulting from any ideas, methods, instructions, or products referred to in the content.

Article

# Mineral Deposition on the Rough Walls of a Fracture

Nathann Teixeira Rodrigues <sup>1</sup>, Ismael S. S. Carrasco <sup>2</sup>, Vaughan R. Voller <sup>3</sup> and Fábio D. A. Aarão Reis <sup>1,\*</sup>

<sup>1</sup> Instituto de Física, Universidade Federal Fluminense, Avenida Litorânea s/n, 24210-340 Niterói RJ, Brazil

<sup>2</sup> International Center of Physics, Institute of Physics, University of Brasília, 70910-900, Brasília, Federal District, Brazil

<sup>3</sup> Department of Civil, Environmental, and Geo- Engineering and Saint Anthony Falls Laboratory, University of Minnesota, 500 Pillsbury Drive SE, Minneapolis, MN 55455, USA

\* Correspondence: fdaar@protonmail.com

**Abstract:** Modeling carbonate growth in fractures and pores is important for understanding carbon sequestration in the environment or when supersaturated solutions are injected into rocks. Here we study the simple but nontrivial problem of calcite growth on fractures with rough walls of the same mineral using kinetic Monte Carlo simulations of attachment and detachment of molecules and scaling approaches. First we consider wedge-shaped fracture walls whose upper terraces are in the same low energy planes and show that the valleys are slowly filled by propagation of parallel monolayer steps in the wedge sides. The growth ceases when the walls reach these low energy configurations, so that a gap between the walls may not be filled. Secondly we consider fracture walls with equally separated monolayer steps (vicinal surfaces with roughness below 1 nm) and show that growth by step propagation will eventually clog the fracture gap. In both cases, scaling approaches predict the times to attain the final configurations as a function of the initial geometry and of the step propagation velocity in the chosen supersaturation. The same reasoning applied to a random wall geometry shows that step propagation leads to lateral filling of surface valleys until the wall reaches the low-energy crystalline plane that has the smallest initial density of molecules. Thus, the final configurations of the fracture walls are much more sensitive to the crystallography than to the roughness or to the local curvature. The framework developed here may be used to determine those configurations, the times to reach them, and the mass of deposited mineral.

**Keywords:** carbon mineralization; calcite; growth; fracture; Kinetic Monte Carlo; surface steps

## 1. Introduction

A promising method for sequestration of atmospheric carbon is the injection of reactive fluids containing CO<sub>2</sub> into mafic or ultramafic rocks because it promotes reactions with silicates and the precipitation of carbonate minerals in the pores [1–5]. However, the success of this method is still limited and the pathways to improve it are unclear due to the large number of open questions ranging from the transport of solutions in time-evolving porous media to the distribution of the carbonates in those media [1]. Similar questions appear in natural processes of mineral dissolution and precipitation that affect porosity and fluid transport [6,7]. These phenomena motivated a large number of experimental and modeling studies in the last decades [8–17].

The initial steps of carbonate growth in rock pores or rock fractures consist of nucleation of crystals on surfaces of primary or secondary minerals [10–16,18–22]. A variety of crystal morphologies may appear, such as compact layers that cover the entire pore surface, isolated growing crystals, or disordered layers with nanoporosity. For instance, in experiments with the flow of supersaturated solutions in microporous quartz columns [12] and in 1 mm diameter plexiglass tubes [23], calcite grains with sizes  $\sim 0.1$ –1 mm were deposited. However, there are also column experiments showing the growth of calcite coatings around sand grains [13,24] and barite layers covering SiO<sub>2</sub> particles [10], which shows that nontrivial mineral-substrate interactions control the shapes of the deposits. Other problems with nontrivial interactions are those with injection of supersaturated solutions of CaCl<sub>2</sub> and NaHCO<sub>3</sub> and calcite growth: the injection into fractured samples containing calcite and dolomite predominantly leads to mineral grain formation on the calcite substrates [14], but the flow in columns with calcite and aragonite grains mixed with glass beads leads to preferential growth of

homogeneous layers on those substrates [11]. In these and other column experiments, preferential growth at the column inlets is generally observed, possibly with fracture sealing, which means that obtaining significant mineralization in the whole pore space may be a difficult task.

The growth of calcite, quartz, and barite on fracture surfaces has been previously addressed with reactive transport models based on hydrodynamic equations of fluid or solute transport and on reaction rate laws obtained in laboratory works [14,17,25–30]. Some of these studies discuss growth patterns formed in the individual pores. The reactive transport equations are very useful to relate observations in several lengthscales, but they do not represent molecular scale processes at crystal surfaces which may be crucial in the initial steps of the mineralization when wetting layers or isolated mineral grains are formed. There are cases in which reactive transport equations cannot properly describe the patterns of dissolving surfaces at nano or microscale even if those equations account for the local surface slope [31]. Instead, techniques such as kinetic Monte Carlo (KMC) simulations and scaling approaches are suitable for the description of crystal growth and dissolution at those scales [32,33]. For instance, they have successfully described stepwaves in dissolving etch pits [34], smoothening of rough surfaces [35], and dissolution rate spectra [36].

Here we address a simple but nontrivial problem of calcite growth in conditions that may be relevant to technological and natural processes: the growth on fracture walls formed by the same mineral and in contact with a solution with approximately uniform saturation. This initial condition of the walls may occur either because a mineral layer has formerly precipitated on those walls or because that was the primary mineral in the sample. The uniform saturation is possible if the advective transport in the fracture gap is sufficiently fast to homogenize the solution while precipitation occurs; this corresponds to a Damköhler number  $\ll 1$  [37]. Although this is a relatively simple case in the scenario of mineral growth in rock fractures, it is an essential step before attempting to model more complex problems.

A combination of kinetic Monte Carlo (KMC) simulations and scaling methods will be used here to determine the evolution of the wall profiles until the growth ceases, the resulting fracture profiles (which are possibly sealed), and the time to attain these final configurations. The nanoscale model considers the random aggregation of molecules coming from the solution and a stochastic model that accurately represents molecule detachment from calcite surfaces [38,39]. The model parameters are calibrated by laboratory values of velocities of propagation of monolayer steps [40–42]. The results are upscaled by considering the crystallographic orientations of the initial wall profiles and those velocities.

## 2. Materials and Methods

### 2.1. Approximation of the Calcite Crystal Structure

The structure of calcite crystals is simplified using the Kossel crystal approximation (simple cubic lattice) [43], in which the lowest energy planes mimic the  $(10\bar{1}4)$  surface of calcite. This approximation was recently used to determine far from equilibrium dissolution rates in alkaline environment which were in excellent agreement with experimental data [38,39]. Each lattice site represents one molecule with an edge length  $a = 0.394\text{nm}$  in order to match the molar volume  $V_M = 3.693 \times 10^{-5} \text{m}^3/\text{mol}$  of the mineral in normal temperature and pressure. The rates of molecule detachment from a surface, given in Sec. 2.3, depend on the numbers  $n$  of nearest neighbors (NNs) which are illustrated in Figure 1. The terms kink, step, and terrace sites are used throughout the text to refer to sites with  $n = 3, 4,$  and  $5$ , respectively.

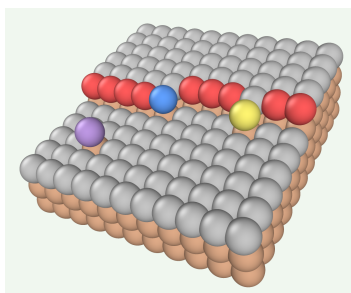


**Figure 1.** A region of a surface in the Kossel crystal where site colors indicate their coordinations:  $n = 1$  in purple,  $n = 2$  in yellow,  $n = 3$  (kink site) in blue,  $n = 4$  (step site) in red,  $n = 5$  (terrace site) in gray, and  $n = 6$  in brown. The sites surrounding this region contain molecules which affect site colors at the boundaries.

## 2.2. Fractures with Rough Walls

In the first model, the walls have a sequence of wedges whose  $xy$  sections are schematically illustrated in Figure 2(a). Each wedge has base length  $l$  ( $x$  direction), height  $h$  ( $z$  direction), and is symmetric under translation in the  $y$  direction. The reference planes  $z = 0$  and  $z = 2h + g$  are indicated at the bases and at the tips of the wedges in Figure 2(a), where  $g$  is the width of the gap between the tips. The wedge angle  $\alpha$  is given by

$$\tan \alpha = \frac{h}{(l/2)}. \quad (1)$$

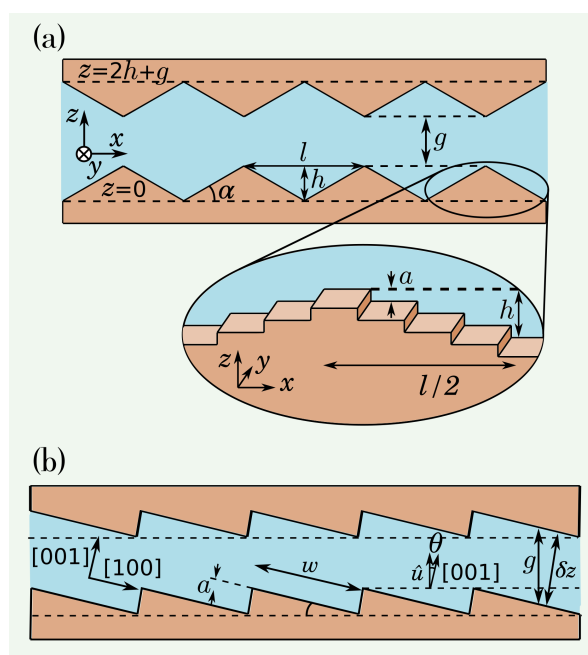


**Figure 2.** (a) Two-dimensional section of a fracture with wedge-shaped walls. The magnified zoom shows a three-dimensional view of a wedge with a small angle  $\theta$ , which is formed by wide terraces separated by monolayer steps (the bottoms and the tips of the wedges belong to two low energy planes of the calcite crystal). (b) Two-dimensional  $xz$  section of a fracture whose walls are vicinal surfaces forming angle  $\theta$  with the  $z$  direction.

The magnified zoom of Figure 2(a) shows that wedges with small slopes ( $h \ll l/2$  or  $\alpha \ll 45^\circ$ ) are formed by low energy  $(0,0,\pm 1)$  terraces separated by monolayer steps of height  $a$ . The terraces at the wedge tips belong to the same low-energy planes  $(0,0,\pm 1)$  and the same occurs with the terraces at the wedge valleys.

The second model considers that the fracture walls are vicinal surfaces with equally separated monolayer steps and terraces of length  $w$  oriented in  $[0,0,\pm 1]$  directions, as illustrated in Figure 2(b). This is a typical configuration of cleaved calcite surfaces [40]. The wall roughness is smaller than  $a \approx 0.4$  nm. The vector normal to the bottom surface is denoted as  $\vec{u}$  and forms an angle  $\theta$  with the  $[00\pm 1]$  direction, so that

$$\tan \theta = \frac{a}{w}. \quad (2)$$

Here we consider only cases of small angles:  $\theta \ll 1$ . The gap  $g$  between the walls is measured along the direction of  $\vec{u}$ , as shown in Figure 2(b). The separation  $\delta z$  between the terraces in the same  $x$  position is

$$\delta z = g \cos \theta. \quad (3)$$

In all geometries, we use the term column to denote the set of molecules of a wall with the same coordinates  $(x, y)$  and varying  $z$ . For small slopes, only the molecule with the largest (smallest)  $z$  of the bottom (top) wall is in contact with the solution.

In Sec. 3.3, a third model with fracture walls with random fluctuations and different crystallographic orientations is analyzed.

### 2.3. Model of Calcite Dissolution and Precipitation

We simulate the dynamics of calcite dissolution and precipitation by sequential events of detachment of calcite molecules (sites) from the crystal surface and attachment of new molecules at that surface.

The detachment model was formerly used to predict accurate values of the far-from-equilibrium dissolution rate of calcite grains and defect-free surfaces [38,39]. The detachment rate depends on the coordination number  $n$  as

$$\begin{aligned} r_n &= \nu \epsilon^n, & n \leq 4, \\ r_5 &= \nu \epsilon^{5.75}, \end{aligned} \quad (4)$$

where  $\nu$  is a characteristic frequency,  $\epsilon = \exp[-E/(k_B T)]$ ,  $E$  is an activation energy,  $k_B$  is the Boltzmann constant, and  $T$  is the temperature. The room temperature parameters considered here are [38]

$$\nu = 3 \times 10^{10} \text{s}^{-1}, \quad \epsilon = 1.4 \times 10^{-3}. \quad (5)$$

The precipitation is assumed to occur through the random incidence of molecules on the columns  $(x, y)$  of the crystal surface. The flow rate  $r^+$  is defined as the average number of incident molecules on each column (bottom or top) per unit of time. This rate depends on the properties of the solution and is expected to be proportional to the product of activities of calcium and carbonate ions. However, the probability that an incident molecule actually attaches to the crystal is the sticking coefficient  $s$  [44], which depends on the properties of the surface and of the incoming ions; with probability  $1 - s$ , the aggregation attempt is rejected. Thus, the attachment rate is  $sr^+$ , where  $s$  may depend on  $r^+$ . This dependence is determined in the Appendix using step propagation velocities from AFM studies.

Chemical equilibrium is achieved when the attachment rate matches the detachment rate of kink sites because the latter dominates the detachment processes [45]. Assuming  $s = 1$  in this equilibrium condition, we have  $r^+ = r_3$ . The saturation ratio  $\Omega$  of the solution indicates the depletion or excess of calcium and carbonate ions relatively to the equilibrium and is expected to be proportional to the flow rate  $r^+$  [45], so that

$$\Omega_{model} = \frac{r^+}{r_3} \quad (6)$$

Here the *model* index indicates that this saturation is defined in terms of kinetic parameters which are expected to be proportional to thermodynamic activities.

The assumption of uniform attachment rates on the crystal surface is reasonable if a solution with constant ion concentrations is flowing through the fracture and if diffusion of those ions is sufficiently fast to homogenize the solution between the surface protrusions and valleys. If the height difference between protrusions and valleys is of  $\sim 1 \mu\text{m}$  and if a diffusion coefficient in solution of order  $10^{-5} \text{ cm}^2/\text{s}$  is considered, the diffusion time across that height is of the order of one millisecond. However, the growth time of a calcite monolayer in our simulations is 1–10 s, which is sufficiently long to warrant the solution equilibration between those points. This justifies the assumption of uniform attachment rates.

#### 2.4. Quantities of Interest and Methods of Solution

The simulations of the lattice model are performed with an extension of the kinetic Monte Carlo algorithm by Meakin and Rosso [46], which is summarized in Ref. [35].

The wedge-shaped fractures typically have 4 wedges with angles  $\alpha$  from  $0.5^\circ$  to  $5^\circ$  and base length  $l$  from 40 nm to  $4 \mu\text{m}$ . The total length of the simulation cell is  $L_x = 4l$  in the  $x$  direction and the width in the  $y$  direction is a constant  $L_y = 40 \text{ nm}$ . Periodic boundaries are considered in the  $x$  and  $y$  direction to avoid spurious effects of crystal edges. The vicinal surfaces have angles  $\theta$  from  $0.5^\circ$  to  $5^\circ$  and total lengths in the  $x$  and  $y$  directions of  $L_x = L_y = 400 \text{ nm}$ .

During the simulations, we compute the numbers of detached and attached molecules, which give the net change  $N(t)$  of the number of molecules in the solid at time  $t$ . The dissolution rate  $k(t)$ , in  $\text{mol}/(\text{m}^2\text{s})$ , is the change in the number of moles of the solid per unit of time and per unit of planar area, i.e. considering the projected area in the  $xy$  plane:

$$k(t) = \frac{\Delta N(t)}{N_A L_x L_y \Delta t}, \quad (7)$$

where  $\Delta N(t)$  is the change in  $N$  in the time interval  $\Delta t$  and  $N_A$  is the Avogadro number.

In the simulations with wedge-shaped walls, we also calculate the ratio between  $N(t)$  and the number  $N_I$  of molecules initially located between the reference planes  $z = 0$  and  $z = 2h + g$  shown in Figure 2(a). The value of  $N_I$  is given as

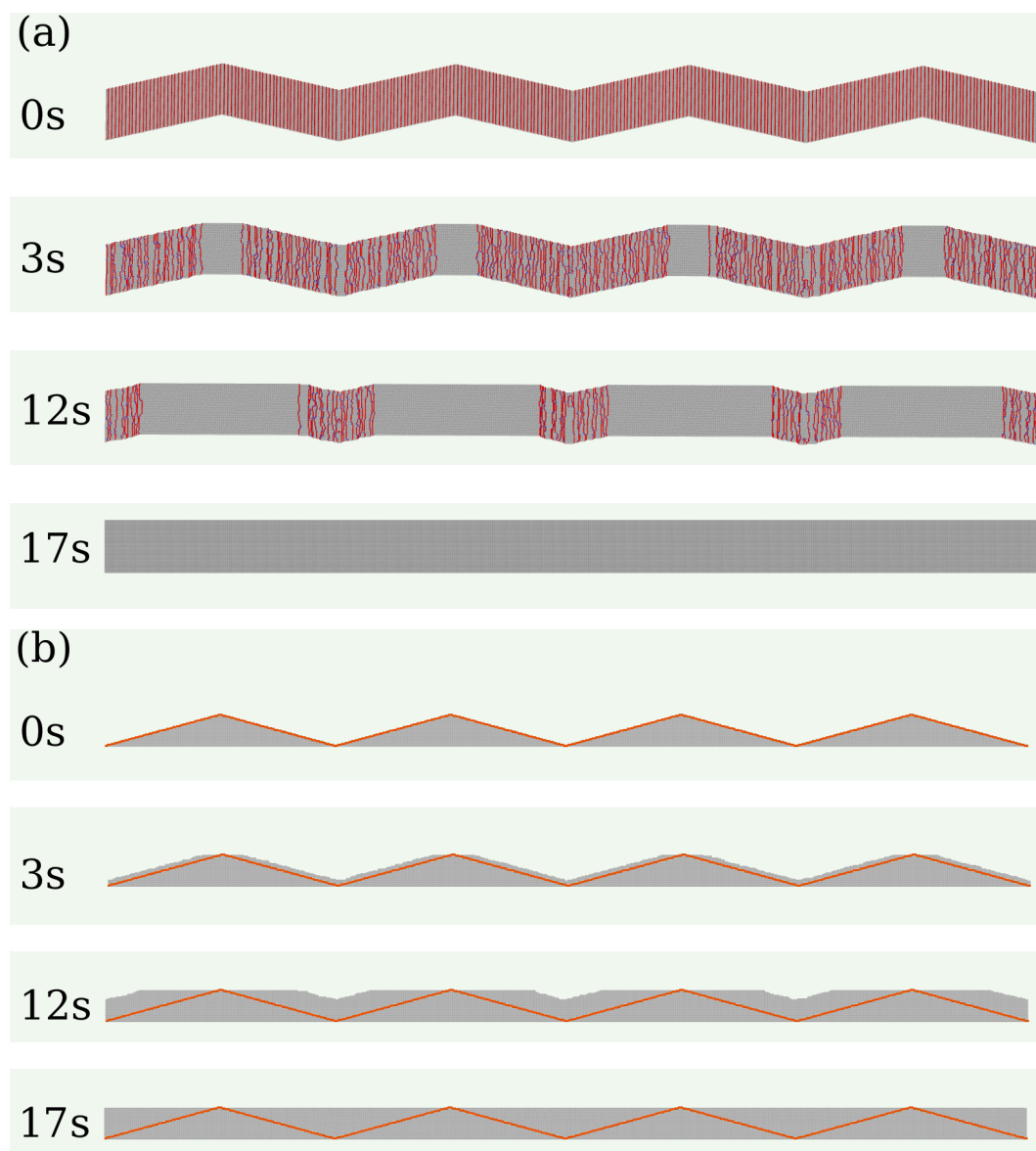
$$N_I = \frac{h L_x L_y}{a^3}. \quad (8)$$

In a regime where growth occurs,  $N(t)/N_I$  is a measure of the fractional filling of the valleys between the surface wedges.

### 3. Results and Discussion

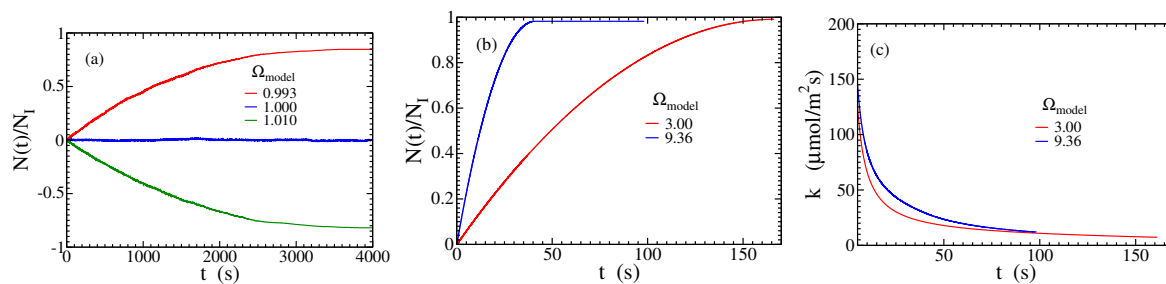
#### 3.1. Growth in the Fracture with Wedge-Shaped Walls

Figure 3(a) shows snapshots of a wedge-shaped wall during calcite growth under supersaturation with  $\Omega_{\text{model}} = 3.00$ . Figure 3(b) shows the corresponding vertical cross-sections ( $xz$  plane). These images show that the initial surface steps propagate laterally towards the center of the valleys between the wedges. This propagation occurs at all depths until opposite steps meet at a valley and form a low-energy plane; the valley then moves up a distance  $a$  (the lattice constant). At the ridges, there is an expansion of the topmost terraces in  $\pm x$  directions. The sharp morphology of the valleys does not change because the steps at all depths propagate with approximately the same velocity; this is revealed by comparison of the growing walls with the initial walls in Figure 3(b). Although the detachment of molecules occurs and competes with the precipitation, no dissolution is visible at the scale of those snapshots.



**Figure 3.** (a) Snapshots of a wall with initial wedge shape, total length of  $400\text{nm}$ , and angle  $\alpha = 15^\circ$ , in solution with  $\Omega_{model} = 3.00$ . (b) Evolution of the cross-section of the crystal in  $xz$  plane. In all panels, the orange lines indicate the projection of the initial walls on the  $xz$  plane.

Figure 4(a) shows the ratio  $N(t)/N_I$  as a function of time for three saturation ratios near or at equilibrium,  $\Omega_{model} = 0.993, 1$ , and  $1.01$ . This shows that the dynamical equilibrium of molecule attachment and detachment is attained with a fine-tuning of the model parameters at  $\Omega_{model} = 1$ . Small deviations from this value lead to dissolution ( $\Omega_{model} < 1$ ) or growth ( $\Omega_{model} > 1$ ) at a global scale in times of minutes to a few hours, despite the competition between the aggregation and detachment of molecules in both cases.



**Figure 4.** Results for growth or dissolution in wedge-shaped fracture walls: (a) Ratio  $N(t)/N_I$  with  $l = 400$  nm and  $\alpha = 5^\circ$  for the saturations indicated in the plot. (b) Ratio  $N(t)/N_I$  with  $l = 4$   $\mu\text{m}$  and  $\alpha = 5^\circ$  for the saturations indicated in the plots. (c) Evolution of the growth rate for the same walls and saturations of (b).

Figure 4(b) shows  $N(t)/N_I$  as a function of time for  $\Omega_{model} = 3.00$  and  $\Omega_{model} = 9.36$ . The positive slopes show that precipitation is dominant over dissolution at all times, but the downward curvatures indicate a slowdown of the growth rate. This occurs because opposite steps are continuously meeting at the valleys between the wedges, so the number of propagating steps that contribute to the growth rate decreases in time; see Figs. 3(a) and 3(b). The process eventually reaches a stationary state with  $N(t)/N_I \approx 1$ , in which the valleys are filled and the walls become flat  $(0,0,\pm 1)$  surfaces. The unit value of this ratio corresponds to the full filling of the valleys and negligible dissolution, which is consistent with the longest-time snapshots in Figs. 3(a)-(b). Figure 4(c) shows the evolution of the growth rate  $k$  for the same parameters of Figure 4(b) and confirms the decrease of that rate.

The time  $t_{st}$  in which the stationary state is attained is defined as the first time in which only terrace sites are present on the surface. The stationary value  $N(t_{st})/N_I$  measured at that time is shown in Figure 5 as a function of  $1/l$  (reciprocal of the length of a wedge) for three wedge angles. The extrapolations to  $1/l \rightarrow 0$  show that  $N(t_{st})/N_I \rightarrow 1$ . This limit is applicable to wedges with microscale lengths, in which  $1/l \leq 0.001$   $\text{nm}^{-1}$ . In these cases, the initial valleys between the edges are fully filled with precipitated mineral, the dissolution of the initial walls is negligible, and the precipitation ceases when the walls become  $(0,0,\pm 1)$  terraces.

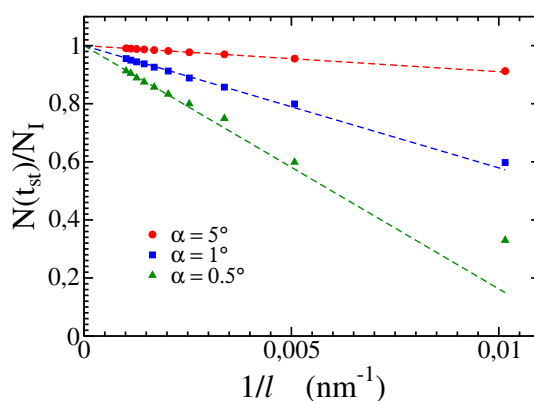


**Figure 5.** Stationary value of  $N(t_{st})/N_I$  as function of  $1/l$  for different angles  $\alpha$ .

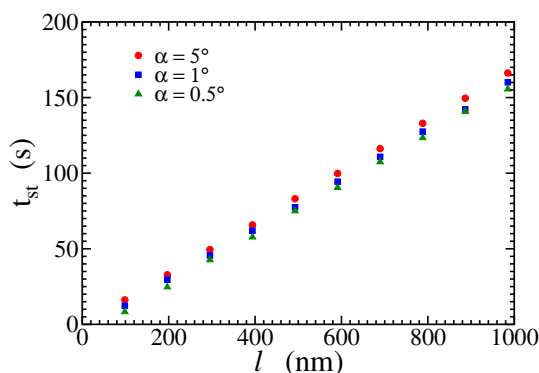
The zero growth rate on  $(0,0,\pm 1)$  surfaces is a consequence of the fast detachment of molecules deposited on terraces, i.e. detachment rate  $r_1$  much larger than the attachment rates  $k^+ = sr^+ = s\Omega_{model}r_3$ , as discussed in the Appendix. Sequential deposition of two molecules at neighboring sites is highly unlikely in these conditions, which prevents crystal nucleation.

Figure 6 shows the time to reach the stationary state as a function of  $l$  for three angles of the wedges and  $\Omega_{model} = 3.00$ . There is a linear relation between these quantities because the complete

filling of the gap between two wedges occurs when the monolayer steps at the ridges meet. Denoting the velocity of those steps as  $v_s$ , it can be estimated as

$$v_s = \frac{(l/2)}{t_{st}}. \quad (9)$$

From the reciprocal of the slopes of fits of Figure 6 and Eq. (9), we obtain  $v_s \approx 3$  nm/s for  $\Omega_{model} = 3.00$ . This result is in good agreement with direct simulation of step propagation for the same saturation ratio, which gives  $v_s \approx 3.007$  nm/s; see Appendix.



**Figure 6.** Stationary times  $t_{st}$  as function of  $l$  for  $\alpha = 0.5^\circ, 1.0^\circ$  and  $5.0^\circ$ .

These results show that the lateral growth by step propagation occurs with approximately the same velocity at all depths of the wedges, from the tips to the valleys. At a hydrodynamic scale, the valleys have the highest surface curvatures [Figure 2(a)], but this does not lead to faster growth at those points. Instead, the valleys slowly move up due to the lateral filling. Moreover, the wedge tips have the lowest curvatures at hydrodynamic scale, but this neither prevents the lateral growth nor favors dissolution because the tips are low-energy terraces at nanoscale.

Thus, at the hydrodynamic scale, step propagation is the mechanism that controls the growth, not the surface curvature. Eq. (9) shows how this mechanism can be used to predict the time in which the precipitation is expected to cease. The mass of deposited material can also be easily calculated from the initial geometry. It is also important to observe that this fracture model [Figure 2(a)] allows the gap of size  $g$  to remain open for fluid flow after the growth ceases. This occurs because the initial tips are aligned in the same low-energy plane of the crystal. This result is valid even if the initial roughness of the walls is large.

As a final note, the above interpretations based on step propagation features are possible because the separation between the steps is large in the studied models (small angles  $\alpha$ ). This parallels the interpretations based on the stepwave model [34], which is able e.g. to describe calcite dissolution rates controlled by etch pitting [47]. However, when monolayer steps are close to each other, their interaction may lead to curvature effects as those observed when grain edges dissolve and become rounded [31].

### 3.2. Growth in the Fracture with Vicinal Surfaces

Here we study mineral growth in fractures whose walls are vicinal surfaces [Figure 2(b)], which have subnanoscale roughness but are not low energy surfaces. Figure 7 shows cross sections of a fracture with  $w = 100a = 40$  nm during the growth. Again, we observe that the gap is slowly filled by the propagation of surface steps, without nucleation of islands or three-dimensional crystals. However, contrary to the previous case, all steps in a wall propagate in the same direction, so they do not meet to form low-energy planes. Thus, the growth ceases only when steps of opposite walls meet and clog the fracture spacing.



**Figure 7.** Evolution of the cross-section of a fracture with vicinal surfaces with terrace length of 40 nm. The orange lines indicate the initial walls.

The time for the fracture gap to be filled can also be calculated from the initial geometry and the step propagation velocity  $v_s$  at the chosen saturation. The average time for deposition of one layer of molecules in each wall is the time for a step to propagate to a distance  $w$ , which is the distance between consecutive steps [Figure 2(b)]:

$$\tau_1 \approx \frac{w}{v_s}. \quad (10)$$

During this time, the walls move a distance  $a$  in the  $z$  direction, so their growth velocity in that direction is

$$v_z = \frac{a}{\tau_1} \approx v_s \tan \theta, \quad (11)$$

where Eq. (2) was used. The gap between the walls is filled when the sum of the displacements of the two walls in the  $z$  direction reaches the initial separation  $\delta z$  [Figure 2(b)]; using Eq. (3) we obtain:

$$\tau_{fill} = \frac{\delta z}{2v_z} = \frac{\delta z}{2v_s \tan \theta} = \frac{g \cos \theta}{2v_s \tan \theta}. \quad (12)$$

Observe that, for small angles  $\theta$ , the separation  $\delta z$  and the gap width  $g$  have approximately the same value [Eq. (3)].

Figure 8 shows the values of the scaled time  $(\tanh \theta)\tau_{fill}$  as a function of the separation  $\delta z$  obtained in KMC simulations for two angles and two saturations. The collapse of the data for the same saturation gives support to the prediction of Eq. (12). From Eq. (12), the reciprocal of the slopes of the linear fits of the plots in Figure 8 are expected to be twice the step propagation velocity. This gives  $v_s = 3.14$  nm/s and  $v_s = 12.63$  nm/s for  $\Omega_{model} = 3.00$  and  $\Omega_{model} = 9.36$ , respectively, both in good agreement with the simulations of step propagation (see Appendix).

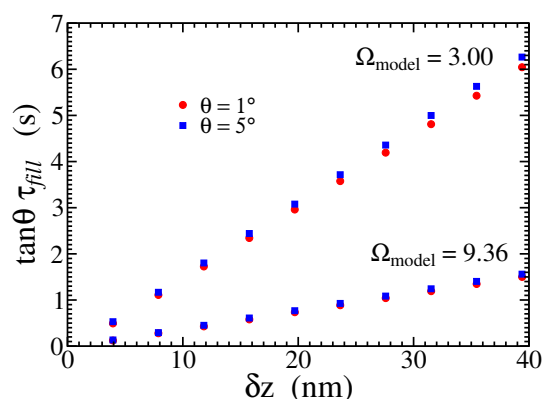


**Figure 8.** Scaled time to fill the gap between the vicinal surfaces as a function of the gap distance for two different angles and saturation ratios.

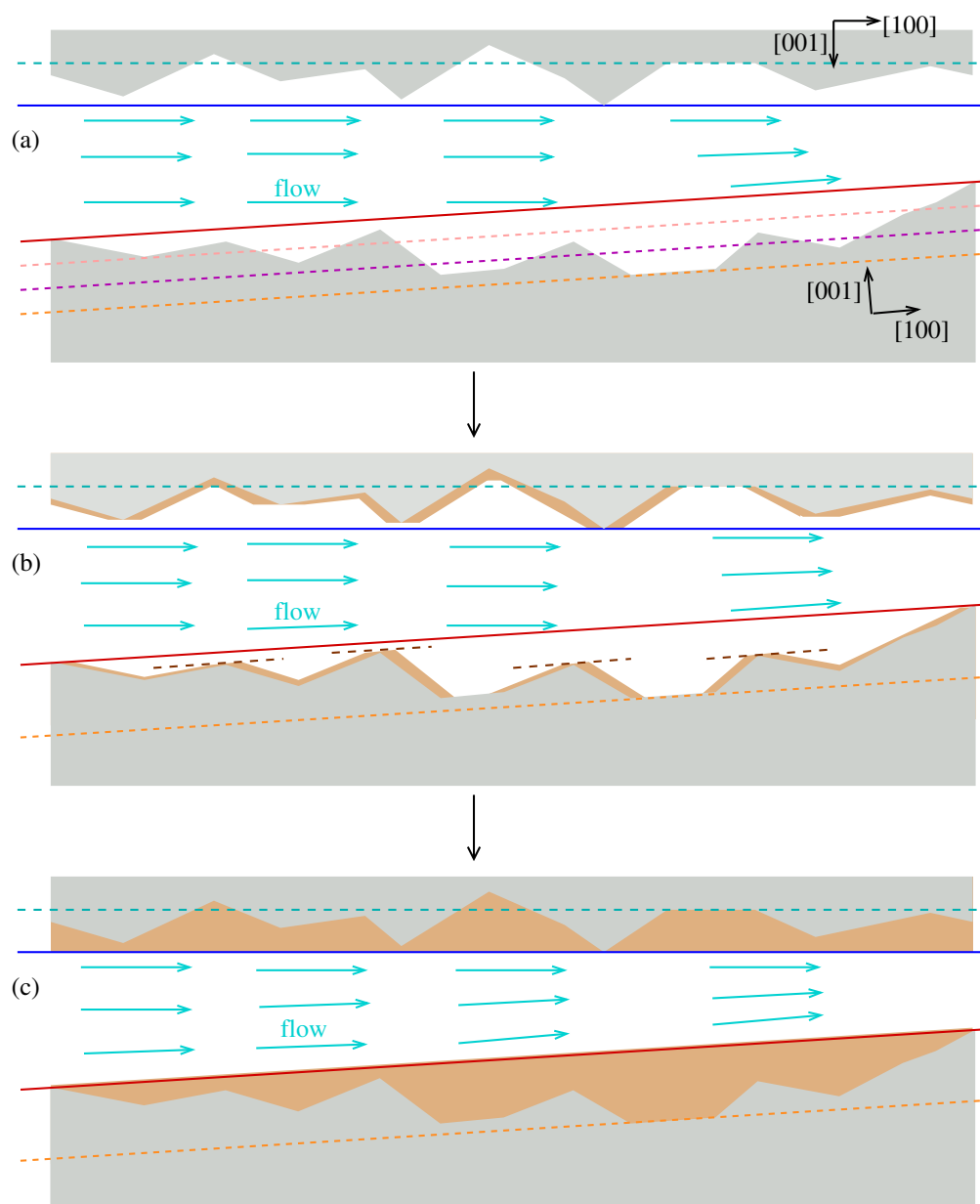
These results confirm the leading role of step propagation when a mineral is deposited in fracture walls. More importantly, they show that the fracture spacing is completely filled in conditions of very small initial roughness, in contrast to the case of rough wedge-shaped walls. This shows that the wall crystallography is much more important than the roughness to predict the final pore shape.

### 3.3. Growth in a Fracture with Rough Surfaces

The growth on fracture walls is controlled by step propagation along the main crystallographic directions and this propagation ends only when steps moving in opposite directions meet and form low-energy terraces. A more general case of an initial fracture with the symmetry in the  $y$  direction is shown in Figure 9(a), with upper and lower crystals aligned in different orientations. The dashed lines across the whole image are some low-energy planes that cross the upper and lower walls. The two solid lines are the low-energy planes that cross the smallest density of molecules of each wall; geometrically, these planes intercept the wall cross sections in a minimal (but non-zero) number of points. The left and right ends of the lower crystal in Figure 9(a) were chosen at two subsequent intersections with the smallest density plane (red line).

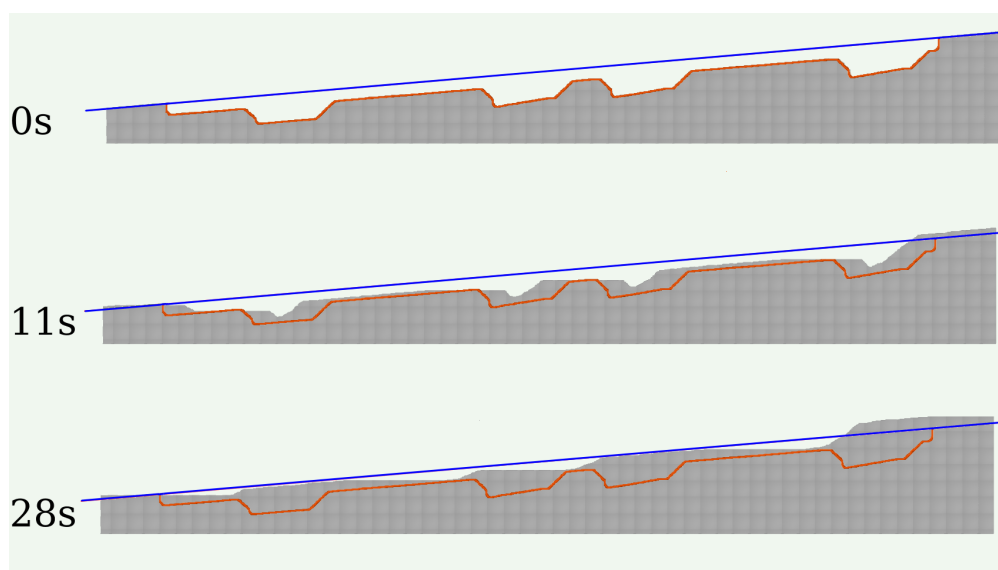
Figure 9(b) shows the walls after some time. In the lowest wall, dashed brown lines passing through the surface tips show that those tips laterally expand to form low-energy terraces, similar to what was observed in the wedge-shaped geometry [Figs. 3(a) and 3(b)]. The valleys may move up but they remain sharp. Similar features are observed in the upper wall. In both walls, observe that some wide valleys are low-energy planes that remain partially exposed in Figure 9(b).

Figure 9(c) shows the configuration in which the two walls become low-energy planes and where no growth occurs. Those configurations are the initial low-energy planes with the smallest density of molecules because the most protuberant steps propagate along those planes until covering the intermediate parts of the surfaces. The velocity of step propagation (which depends on the saturation ratio) and the distance between those protuberances can be directly used to estimate the deposition time in that region. The average depth below those protuberances can be used to estimate the mass of deposited material.



**Figure 9.** Expected sequence of configurations of a fracture with initially rough walls during calcite growth. Low-energy planes are indicated by parallel lines, with increasing initial density of molecules in the following order in the lower crystal: red solid line; pink dashed line; magenta dashed line; orange dashed line. Brown dashed lines in the intermediate time (b) are drawn through terraces formed around local surface peaks. Flow lines in the fracture spacing are schematically represented.

We also performed simulations of calcite growth on a wall with features similar to those of the lower wall of Figure 9(a). The evolution of this simulated wall is shown in Figure 10 and confirms the predictions of the previous schematic images. The only difference is that some steps enter at the right side in Figure 10 because the highlighted region is part of a larger crystal.



**Figure 10.** Evolution of the cross-section of a rough wall during calcite growth. The initial configuration of the wall is indicated by the orange line.

#### 4. Conclusions

The success of the permanent carbon sequestration process based on sub-surface mineralization critically depends on the dissolution and precipitation process within the fractures and pores of the host reservoir rocks. Under what conditions will mineralization occur on a given surface? How do these processes modify the transport processes? As mineralization occurs, is the flow of the charge through the rock matrix maintained or is it shut off? The work presented here has provided some initial clues to address these questions, informing potential constitutive relationships at nano and microscale that may be used in large (field) scale models aimed at predicting the permanent storage potential of a given reservoir.

Calcite growth was studied on fractures with walls of the same mineral and different roughness patterns, with special emphasis on (large roughness) wedge-shaped walls and (low roughness) vicinal surfaces. Kinetic Monte Carlo simulations of a model of attachment and detachment of molecules were performed and scaling approaches were used to interpret the numerical data, predict the final configurations of the deposits, and the time to reach them. The Kossel crystal approximation was used, in which the low-energy ( $10\bar{1}4$ ) surface of calcite is represented by  $(0,0,\pm 1)$  planes.

The initially wedge-shaped walls had tips in the form of narrow terraces in the same low-energy plane and their lateral sides were terraces separated by monolayer steps (for small wedge angles). Growth took place by propagation of all those steps towards the valleys between the wedges. When opposite steps immediately above a valleys meet, they form a low-energy plane at that valley; the height of the valley is displaced of one lattice constant, while the other steps continue to propagate. The growth ceases when opposite steps coming from consecutive tips meet and the walls form a low-energy plane, possibly leaving an open gap in the center of fracture which allows fluid flow. The time to reach this final configuration can be calculated from the distance between those tips and the velocity of step propagation at the given supersaturation.

The walls with vicinal surfaces have equally separated monolayer steps and roughness below 1 nm. Growth also occurs by step propagation until opposite steps at opposite walls meet, which leads to pore clogging. We showed that the time to reach this configuration can be calculated from the initial distance between the steps, the gap width, and the step velocity.

We finally considered the case of fractures with random wall geometries and with possibly different crystalline orientations in the upper and the lower walls. In each wall, step propagation is also responsible for the lateral filling of surface valleys until the wall reaches the low-energy plane that has the smallest initial density of molecules. The deposited mass may be estimated by the average

height of the valleys below this plane. This shows that the wall crystallography controls the growth, while the roughness or the local curvature are not suitable quantities to predict the final configurations at nanoscale. However, the framework based on the step propagation mechanism may be used to determine those configurations, the times to reach them, and the mass of deposited mineral.

**Author Contributions:** Conceptualization, F.D.A.A.R., V.R.V.; methodology, N.T.R., I.S.S.C., F.D.A.A.R.; software, N.T.R., I.S.S.C.; validation, N.T.R., I.S.S.C.; formal analysis, N.T.R., I.S.S.C., V.R.V. and F.D.A.A.R.; investigation, N.T.R., I.S.S.C., F.D.A.A.R.; resources, F.D.A.A.R., V.R.V.; data curation, N.T.R., I.S.S.C.; writing—original draft preparation, F.D.A.A.R.; writing—review and editing, N.T.R., I.S.S.C., V.R.V. and F.D.A.A.R.; visualization, N.T.R., I.S.S.C., F.D.A.A.R.; supervision F.D.A.A.R.; project administration, F.D.A.A.R.; funding acquisition, F.D.A.A.R., I.S.S.C., V.R.V.. All authors have read and agreed to the published version of the manuscript.

**Funding:** VRV is supported by the Center on Geo-processes in Mineral Carbon Storage, an Energy Frontier Research Center funded by the U.S. Department of Energy, Office of Science, Basic Energy Sciences at the University of Minnesota under award #DE-SC0023429. NRT is supported by the Brazilian agency FAPERJ (E-26/204.396/2021). ISSC is supported by the Brazilian agency FAPDF (00193-00001817/2023-43). FDAAR is supported by the Brazilian agencies CAPES (PrInt 88887.310427/2018-00), CNPq (442233/2023-0, 305570/2022-6), and FAPERJ (E-26/210.062/2023, E-26/201.050/2022).

**Data Availability Statement:** The data presented in this study are available on request from the corresponding author.

**Conflicts of Interest:** The authors declare no conflicts of interest.

## Appendix A

Here we determine the sticking coefficient  $s$  of the model of molecule aggregation.

The equilibrium of dissolution and precipitation is well established by the relation  $r^+ = r_3$  [45], so  $s = 1$  is a reasonable assumption in this condition. Growth occurs for  $r^+ > r_3$  and  $s$  depends on the physical properties of the growing surface. For very rapid growth,  $r^+ \gg r_3$ , the surface properties are determined by the freshly deposited material and we assume that those properties become independent of the growth rate in that limit. Thus we propose a simple relation in which  $s$  saturates for large  $r^+$ :

$$s = 1 + c \left[ e^{-\lambda(r^+ - r_3)} - 1 \right], \quad (\text{A1})$$

where  $c$  and  $\lambda$  are constants and  $r_3$  is given by Eqs. (4) and (5). For  $r^+ - r_3 \gg 1/\lambda$ ,  $s$  converges to the constant value  $1 - c$ .

Using several values of  $c$  and  $\lambda$ , we performed room temperature simulations on large surfaces with monolayer steps, i.e. surfaces with the initial geometry of the walls in Figure 2(b) and  $w \gg a$ . Figure A1 shows the evolution of a region of the surface for  $\Omega_{\text{model}} = 3.00$ ,  $c = 0.62$ , and  $\lambda = 5.2 \times 10^{-3}$  [Eqs. (6) and (A1)]; the choice of these parameters will be justified below. The initial surface step propagates independently and has low roughness. There is no observable detachment of molecules on the terraces separating the steps; whenever this occurs, the pit is rapidly filled by attachment of a molecule from the solution. Similar results are obtained in a broad range of model parameters. This is in qualitative agreement with laboratory studies [41,42].

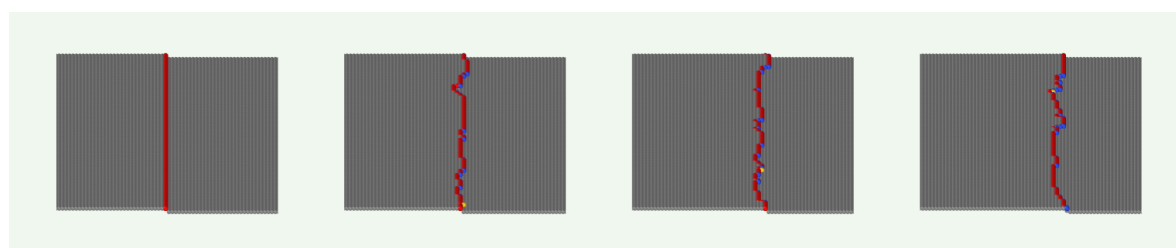


**Figure A1.** Snapshots of a growing surface with initially separated monolayer steps ( $w/a = 256$ ) for  $\Omega_{\text{model}} = 3.00$ ,  $c = 0.62$ , and  $\lambda = 5.2 \times 10^{-3}$ .

Notably, these results are not trivial from the point of view of stochastic growth modeling. If molecule detachment is absent, the random aggregation produces surfaces with Poisson distributions of heights and time increasing roughness (random deposition model) [48,49]. Thus, the smooth step propagation and absence of crystal nucleation on terraces is possible only because the detachment rates of molecules with low coordinations ( $n = 1$  and  $2$ ) are large compared to deposition rates. For instance, the attachment rate is  $k^+ = sr^+ = s\Omega_{model}r_3 = s\Omega_{model}\nu\epsilon^3$  [Eqs. (4) and (6)], which is in the range  $10^2$ – $10^3$   $s^{-1}$  for the saturations considered here. However, the molecules attached on the  $(0,0,\pm 1)$  terraces have a single NN ( $n = 1$ ), so their detachment rate is  $r_1 = \nu\epsilon \sim 10^7$   $s^{-1}$ , which is much larger than  $k^+$ . In simple words, in this model with random aggregation, the growth of smooth surfaces is possible only because  $\epsilon \ll 1$  in Eq. (5).

In a recent work [38], the detachment rates of the model [Eqs. (4) and (5)] were determined by the velocities of dissolving monolayer steps of  $(10\bar{1}4)$  calcite surfaces measured by AFM [40]. Thus, here we will determine the parameters of the sticking coefficient for aggregation [Eq. (A1)] by velocities of growing steps measured by the same technique [41,42]. Since we adopted the Kossel crystal approximation, we will use average values of velocities of acute and obtuse steps of  $(10\bar{1}4)$  surfaces.

The comparison with AFM results of Sand et al [42] for  $\Omega \approx 4$  and  $\Omega \approx 10$  gives  $c = 0.62$  and  $\lambda = 5.2 \times 10^{-3}$ . Figure A2 shows the velocities obtained with these parameters as a function of the saturation ratio  $\Omega_{model}$ , the AFM velocities obtained in that work, and the velocity obtained by Hong et al [41] for  $\Omega \approx 8$ . The good agreement shows the reliability of the model in the regime where molecule attachment dominates ( $r^+ > r_3$ ).

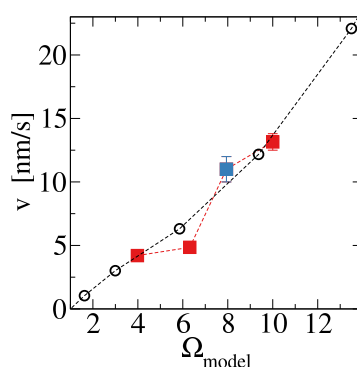


**Figure A2.** Monolayer step velocity as a function of the saturation ratio obtained in simulations (black circles) and in AFM studies (blue filled squares [41] and red filled squares [42]).

For the simulation of deposition in rough fractures, the results for two saturation values are particularly important:  $v_s = 3.007 \pm 0.004$  nm/s for  $\Omega_{model} = 3.00$ ;  $v_s = 12.170 \pm 0.005$  nm/s for  $\Omega_{model} = 9.36$ .

## References

1. Jun, Y.; Zhang, L.; Min, Y.; Li, Q. Nanoscale Chemical Processes Affecting Storage Capacities and Seals during Geologic CO<sub>2</sub> Sequestration. *Acc. Chem. Res.* **2017**, *50*, 1521–1529. doi:10.1021/acs.accounts.6b00654.
2. Xu, R.; Li, R.; Ma, J.; He, D.; Jiang, P. Effect of Mineral Dissolution/Precipitation and CO<sub>2</sub> Exsolution on CO<sub>2</sub> transport in Geological Carbon Storage. *Acc. Chem. Res.* **2017**, *50*, 2056–2066. doi:10.1021/acs.accounts.6b00651.
3. Jiang, H.; Economou, I.G.; Panagiotopoulos, A.Z. Molecular Modeling of Thermodynamic and Transport Properties for CO<sub>2</sub> and Aqueous Brines. *Acc. Chem. Res.* **2017**, *50*, 751–758. doi:10.1021/acs.accounts.6b00632.
4. Linke, T.; Oelkers, E.H.; Möckel, S.C.; Gislason, S.R. Direct evidence of CO<sub>2</sub> drawdown through enhanced weathering in soils. *Geochem. Persp. Lett.* **2024**, *30*, 7–12. doi:10.7185/geochemlet.2415.
5. Oelkers, E.H.; Gislason, S.R. Carbon Capture and Storage: From Global Cycles to Global Solutions. *Geochemical Perspectives* **2023**, *12*, 179–349.

6. Putnis, A. Transient Porosity Resulting from Fluid-Mineral Interaction and its Consequences. In *Reviews in Mineralogy and Geochemistry*; Mineralogical Society of America, 2015; Vol. 80, pp. 1–23. doi:10.2138/rmg.2015.80.01.
7. Addassi, M.; Hoteit, H.; Oelkers, E.H. The impact of secondary silicate mineral precipitation kinetics on CO<sub>2</sub> mineral storage. *Int. J. Greenhouse Gas Ctrl.* **2024**, *131*, 104020. doi:10.1016/j.ijggc.2023.104020.
8. Luquot, L.; Gouze, P. Experimental determination of porosity and permeability changes induced by injection of CO<sub>2</sub> into carbonate rocks. *Chem. Geol.* **2009**, *265*, 148–159.
9. Luquot, L.; Rodriguez, O.; Gouze, P. Experimental Characterization of Porosity Structure and Transport Property Changes in Limestone Undergoing Different Dissolution Regimes. *Transp. Porous Med.* **2014**, *101*, 507–532.
10. Godinho, J.R.A.; Gerke, K.M.; Stack, A.G.; Lee, P.D. The dynamic nature of crystal growth in pores. *Sci. Rep.* **2016**, *6*, 33086. doi:10.1038/srep33086.
11. Noiriél, C.; Steefel, C.I.; Yang, L.; Bernard, D. Effects of pore-scale precipitation on permeability and flow. *Adv. Water Resour.* **2016**, *95*, 125–137. doi:10.1016/j.advwatres.2015.11.013.
12. Godinho, J.R.; Withers, P.J. Time-lapse 3D imaging of calcite precipitation in a microporous column. *Geochim. Cosmochim. Acta* **2018**, *222*, 156–170. doi:10.1016/j.gca.2017.10.024.
13. Baek, S.; Hong, J.; Kim, K.Y.; Yeom, S.; Kwon, T. X-Ray Computed Microtomography Imaging of Abiotic Carbonate Precipitation in Porous Media From a Supersaturated Solution: Insights Into Effect of CO<sub>2</sub> Mineral Trapping on Permeability. *Water Resour. Res.* **2018**, *55*, 3835–3855. doi:10.1029/2018WR023578.
14. Noiriél, C.; Seigneur, N.; Guern, P.L.; Lagneau, V. Geometry and mineral heterogeneity controls on precipitation in fractures: An X-ray micro-tomography and reactive transport modeling study. *Adv. Water Resour.* **2021**, *152*, 103916. doi:10.1016/j.advwatres.2021.103916.
15. Nooraiepour, M.; Masoudi, M.; Shokri, N.; Hellevang, H. Probabilistic Nucleation and Crystal Growth in Porous Medium: New Insights from Calcium Carbonate Precipitation on Primary and Secondary Substrates. *ACS Omega* **2021**, *6*, 28072–28083. doi:10.1021/acsomega.1c04147.
16. Depp, C.T.; Miller, Q.R.S.; Crum, J.V.; Horner, J.A.; Schaef, H.T. Pore-Scale Microenvironments Control Anthropogenic Carbon Mineralization Outcomes in Basalt. *ACS Earth Space Chem.* **2022**, *6*, 2836–2847. doi:10.1021/acsearthspacechem.2c00165.
17. Steefel, C.I.; Hu, M. Reactive transport modeling of mineral precipitation and carbon trapping in discrete fracture networks. *Water Resour. Res.* **2022**, *58*, e2022WR032321. doi:10.1029/2022WR032321.
18. Cil, M.B.; Xie, M.; Packman, A.I.; Buscarnera, G. Solute mixing regulates heterogeneity of mineral precipitation in porous media. *Geophys. Res. Lett.* **2017**, *44*, 6658–6666. doi:10.1002/2017GL073999.
19. Wang, Y.; Zeng, M.; Meldrum, F.C.; Christenson, H.K. Using Confinement To Study the Crystallization Pathway of Calcium Carbonate. *Cryst. Growth Des.* **2017**, *17*, 6787–6792. doi:10.1021/acs.cgd.7b01359.
20. Seyyedi, M.; Mahmud, H.K.B.; Verrall, M.; Giwelli, A.; Esteban, L.; Ghasemizariani, M.; Clennell, B. Pore Structure Changes Occur During CO<sub>2</sub> Injection into Carbonate Reservoirs. *Sci. Rep.* **2020**, *10*, 3624. doi:10.1038/s41598-020-60247-4.
21. Ozotta, O.; Kolawole, O.; Malki, M.L.; Ore, T.; Gentzis, T.; Fowler, H.; Liu, K.; Ostadhassan, M. Nano- to macro-scale structural, mineralogical, and mechanical alterations in a shale reservoir induced by exposure to supercritical CO<sub>2</sub>. *Applied Energy* **2022**, *326*, 120051. doi:10.1016/j.apenergy.2022.120051.
22. Li, X.; Nienhuis, E.T.; Nagurney, A.B.; Miller, Q.R.S.; Zhang, X.; Schaef, H.T. Resolving Nanoscale Processes during Carbon Mineralization Using Identical Location Transmission Electron Microscopy. *Environ. Sci. Technol. Lett.* **2024**, *11*, 79–88. doi:10.1021/acs.estlett.3c00699.
23. Jaho, S.; Sygouni, V.; Rokidi, S.G.; Parthenios, J.; Koutsoukos, P.G.; Paraskeva, C.A. Precipitation of Calcium Carbonate in Porous Media in the Presence of n-Dodecane. *Cryst. Growth Des.* **2016**, *16*, 6874–6884. doi:10.1021/acs.cgd.6b01048.
24. Li, X.; Yang, X. Effects of physicochemical properties and structural heterogeneity on mineral precipitation and dissolution in saturated porous media. *Appl. Geochem.* **2022**, *146*, 105474.
25. Li, X.; Huang, H.; Meakin, P. Level set simulation of coupled advection-diffusion and pore structure evolution due to mineral precipitation in porous media. *Water Resour. Res.* **2008**, *44*, W12407. doi:10.1029/2007WR006742.
26. Deng, H.; Tournassat, C.; Molins, S.; Claret, F.; Steefel, C.I. A pore-scale investigation of mineral precipitation driven diffusivity change at the column-scale. *Water Resour. Res.* **2021**, *57*, e2020WR028483. doi:10.1029/2020WR028483.

27. Deng, H.; Gharasoo, M.; Zhang, L.; Dai, Z.; Hajizadeh, A.; Peters, C.A.; Soullaine, C.; Thullner, M.; Van Cappellen, P. A perspective on applied geochemistry in porous media: Reactive transport modeling of geochemical dynamics and the interplay with flow phenomena and physical alteration. *Appl. Geochem.* **2022**, *146*, 105445. doi:10.1016/j.apgeochem.2022.105445.
28. Wetzel, M.; Kempka, T.; Kühn, M. Hysteresis in permeability evolution simulated for a sandstone by mineral precipitation and dissolution. *Adv. Geosci.* **2022**, *58*, 1–10. doi:10.5194/adgeo-58-1-2022.
29. Yang, F.; Yuan, K.; Stack, A.G.; Starchenko, V. Numerical Study of Mineral Nucleation and Growth on a Substrate. *ACS Earth Space Chem.* **2022**, *6*, 1655–1665. doi:10.1021/acsearthspacechem.1c00376.
30. Späth, M.; Nestler, B. Permeability evolution in open fractures during precipitation and dissolution - A phase-field study. *Adv. Water Resour.* **2023**, *182*, 104563. doi:10.1016/j.advwatres.2023.104563.
31. Rodrigues, N.T.; Carrasco, I.S.S.; Reis, F. Step propagation controls pore shape evolution when mineral walls dissolve under saturation gradients. *Geochim. Cosmochim. Acta* **2024**, *379*, 219–232. doi:10.1016/j.gca.2024.05.028.
32. Michely, T.; Krug, J. *Islands, Mounds, and Atoms*; Springer, 2003.
33. Evans, J.W.; Thiel, P.A.; Bartelt, M.C. Morphological evolution during epitaxial thin film growth: Formation of 2D islands and 3D mounds. *Surf. Sci. Rep.* **2006**, *61*, 1–128. doi:10.1016/j.surfrep.2005.08.004.
34. Lasaga, A.C.; Luttge, A. Variation of Crystal Dissolution Rate Based on a Dissolution Stepwave Model. *Science* **2001**, *291*, 2400–2404. doi:10.1126/science.1058173.
35. de Assis, T.A.; Reis, F.D.A.A. Dissolution of minerals with rough surfaces. *Geochim. Cosmochim. Acta* **2018**, *228*, 27–41. doi:10.1016/j.gca.2018.02.026.
36. Fischer, C.; Luttge, A. Beyond the conventional understanding of water-rock reactivity. *Earth. Planet. Sci. Lett.* **2017**, *457*, 100–105. doi:10.1016/j.epsl.2016.10.019.
37. Fogler, H.S. *Elements of chemical reaction engineering*, 4th ed ed.; Prentice Hall PTR international series in the physical and chemical engineering sciences, Prentice Hall PTR, 2006.
38. Carrasco, I.S.S.; Reis, F.D.A.A. Modeling the kinetics of calcite dissolution in neutral and alkaline solutions. *Geochim. Cosmochim. Acta* **2021**, *292*, 271–284. doi:10.1016/j.gca.2020.09.031.
39. Carrasco, I.S.S.; Machado, E.A.; Reis, F.D.A.A. Simulations of Dissolution of Initially Flat Calcite Surfaces: Retreat Velocity Control and Surface Roughness Scaling. *ACS Earth Space Chem.* **2021**, *5*, 2755–2767. doi:10.1021/acsearthspacechem.1c00153.
40. Shiraki, R.; Rock, P.A.; Casey, W.H. Dissolution Kinetics of Calcite in 0.1M NaCl Solution at Room Temperature: An Atomic Force Microscopic (AFM) Study. *Aquatic Geochem.* **2000**, *6*, 87–108. doi:10.1023/A:1009656318574.
41. Hong, M.; Teng, H.H. Implications of solution chemistry effects: Direction-specific restraints on the step kinetics of calcite growth. *Geochim. Cosmochim. Acta* **2014**, *141*, 228–239. doi:10.1016/j.gca.2014.06.023.
42. Sand, K.K.; Tobler, D.J.; Dobberschütz, S.; Larsen, K.K.; Makovicky, E.; Andersson, M.P.; Wolthers, M.; Stipp, S.L.S. Calcite Growth Kinetics: Dependence on Saturation Index,  $\text{Ca}_2^+:\text{CO}_3^{2-}$  Activity Ratio, and Surface Atomic Structure. *Cryst. Growth Des.* **2016**, *16*, 3602–3612. doi:10.1021/acs.cgd.5b01792.
43. Lasaga, A.C.; Blum, A.E. Surface chemistry, etch pits and mineral-water reactions. *Geochim. Cosmochim. Acta* **1986**, *50*, 2363–2379.
44. Kolasinski, K.W. *Surface Science: foundations of catalysis and nanoscience*, 3rd ed ed.; John Wiley & Sons, 2012.
45. Lasaga, A.C.; Luttge, A. Mineralogical approaches to fundamental crystal dissolution kinetics. *Am. Mineral.* **2004**, *89*, 527–540.
46. Meakin, P.; Rosso, K.M. Simple kinetic Monte Carlo models for dissolution pitting induced by crystal defects. *J. Chem. Phys.* **2008**, *129*, 204106. doi:10.1063/1.3021478.
47. Bouissonnié, A.; Daval, D.; Marinoni, M.; Ackerer, P. From mixed flow reactor to column experiments and modeling: Upscaling of calcite dissolution rate. *Chem. Geol.* **2018**, *487*, 63–75. doi:10.1016/j.chemgeo.2018.04.017.
48. Barabási, A.L.; Stanley, H.E. *Fractal Concepts in Surface Growth*; Cambridge University Press: New York, USA, 1995.
49. Krug, J. Origins of scale invariance in growth processes. *Adv. Phys.* **1997**, *46*, 139–282.

**Disclaimer/Publisher's Note:** The statements, opinions and data contained in all publications are solely those of the individual author(s) and contributor(s) and not of MDPI and/or the editor(s). MDPI and/or the editor(s) disclaim responsibility for any injury to people or property resulting from any ideas, methods, instructions or products referred to in the content.